A Novel Multiparameter RFID Sensing Characteristic Study Using Varactor Diode and Digital Control Coding Method

Yaming Xie, Jiuyi Hao, Zhichong Wan, Guochun Wan, and Liyu Xie

***Abstract*— This article proposes a multiparameter radio frequency identification (RFID) sensor with two controllable coding structures. The sensor integrates the ability of strain and humidity detection and is suitable for the field of structural health monitoring (SHM). The sensor is equipped with three S-shaped structures and one rectangular structure, two S-shaped structures are used as encoding units, one S-shaped structure is used as a humidity detection unit, and the rectangular structure is used as a strain unit. These structures are made on a Rogers RO3003 dielectric substrate. Controllable coding is achieved by changing the capacitance value of the varactor diode. A single coding unit can achieve a coding value of more than 2 bits. Compared with the traditional coding structure, the coding information capacity is improved, which is more suitable for distributed SHM scenarios that require multiple sensors. The digital control circuit is designed on the flexible printed circuit (FPC), which has the characteristics of bendability. It is mainly composed of a microcontroller, Bluetooth, varactor diodes, and other components, and can realize the wireless control function of the coding unit. A broadband antenna is further designed to match the working frequency band of the sensor. Experimental verification shows that the micro-strain of the strain unit is linearly related to its resonant frequency, and the humidity sensitivity is 193.92 kHz/%RH at a relative humidity (RH) of 33.7%–81.2%. The two encoding units can be controlled wirelessly to achieve 25-bit coding while having the advantages of small size and low cost. In the future, this method can be combined with self-powered devices and Internet of Things (IoT) gateways to achieve long-term state control of multiple sensors, providing a new method for SHM applications.**

***Index Terms*— Humidity detection, radio frequency identification (RFID), strain detection, structural health monitoring (SHM), varactor diode, wireless digital control circuit.**

I. INTRODUCTION

BUILDINGS, bridges, and other facilities will experience deformation, cracking, and erosion over the years due to environmental erosion and long-term loads [1]. In order to avoid the above-mentioned conditions leading to disasters that threaten people's lives and property safety, buildings need to be maintained and repaired in a timely manner. If structural health monitoring (SHM) can be performed on buildings and targeted protection and management can be carried out, the life of the buildings can be effectively extended. In the field of SHM, traditional non-destructive detection mainly uses visual, ultrasonic, and electromagnetic technologies [2], [3], [4]. However, most of these technologies are active wired systems. Considering the size and complexity of large structures, the deployment, maintenance, and debugging of these systems are very cumbersome. At the same time, there are disadvantages of high cost and long measurement time. In recent years, chipless radio frequency identification (RFID) technology has developed rapidly in the field of SHM. Compared with chip-based RFID, chipless RFID has been more widely studied due to its lower cost [5], [6]. This technology uses radio waves to identify remote chipless tags and extract information such as cracks and strains stored in the tag capture circuit structure from the backscattered waves.

For RFID strain sensors, chip-based rectangular patch antennas were initially used as strain sensors, which can simultaneously detect stress and gaps on the surface of the test piece [7]. There are many methods for chipless strain sensing. Mita and Takhira [8] used a mechanical structure to design a strain sensor that detects strain magnitude by stretching the elastic bending of plastic materials, but it has the problem of only storing peak strain values. Watanabe [9] used the characteristics of the change in the tag resonant frequency under different strain conditions to design a strain sensor using a millimeter wave chipless RFID tag. The shape of the strain sensor tag was optimized using the time-domain finite difference method and microgenetic algorithm to maximize the sensitivity of the resonant frequency to strain. Yi et al. [10] designed a passive wireless RFID surface strain and crack detection sensor by studying the sensitivity of the RFID strain sensing antenna under changes in the dielectric constant, thereby enhancing the sensitivity of strain detection.

At present, the focus of SHM is still on the changes in mechanical and dynamic properties, such as strain [11], crack [12], relative position [13], displacement [14], and acceleration [15]. The monitoring of physical parameters of the environment in which the structure is located, such as humidity, pH value, and other parameters, has not been fully studied. The working environment of large buildings is uncertain, and

Received 26 July 2024; revised 15 November 2024; accepted 5 December 2024. Date of publication 3 March 2025; date of current version 18 March 2025. This work was supported by the National Natural Science Foundation of China (Multiple Sensitization Mechanisms and Multi-Parameter Sensing Principles of Passive Wireless Intelligent Aggregates) under Project 52378311. The Associate Editor coordinating the review process was Dr. Lei Mao. *(Corresponding author: Guochun Wan.)*

Yaming Xie, Jiuyi Hao, Zhichong Wan, and Guochun Wan are with the Department of Electronic Science and Technology, Tongji University, Shanghai 200092, China (e-mail: 2410215@tongji.edu.cn; 2432305@tongji.edu.cn; wanzhichong@tongji.edu.cn; wanguochun@tongji.edu.cn).

Liyu Xie is with the Department of Disaster Mitigation for Structures, Tongji University, Shanghai 200092, China (e-mail: liyuxie@tongji.edu.cn).

Digital Object Identifier 10.1109/TIM.2025.3547464

their structures are susceptible to damage from cyclic loads and chemical corrosion. Damage to mechanical structures will reduce the mechanical properties of load-bearing materials, and the main feature of early structural damage is the degree of structural strain [16]. Therefore, strain detection is important for large infrastructures. In addition, environmental humidity is one of the key reasons leading to structural degradation. For metal structures, a long-term high-humidity environment will aggravate the corrosion of the structures [17]. For wooden buildings, a high-humidity environment will cause damage to the wooden structures [18]. Therefore, it is much needed to monitor the humidity while testing the mechanical parameters of the structure. Liu and Chen [19] designed an RFID sensor that integrates humidity and coding by combining polyvinyl acetate film and flexible substrate, which provides a good idea for the methodology of temperature and humidity monitoring. Hu et al. [20] covered the sensor with Kapton film for humidity detection, used polydimethylsiloxane that is insensitive to humidity as the encapsulation layer of the coding bit, and designed a 3-bit coded RFID humidity sensor, which reduced the interference of humidity on the coding bit.

With the development of the civil industries, more sensors are needed in the SHM field, so researchers have begun to try to add coding functions to RFID sensors. Vena et al. [21] proposed a new hybrid coding technology that combines phase deviation and frequency position coding. Using five resonators in small size can obtain a coding capacity of more than 22 bits, exploring the coding capacity of coded RFID tags. Chen et al. [22] designed a 4-bit coded multibranch U-shaped RFID strain sensor, which improved the ability to distinguish sensors, but had the disadvantage of fixed coding and inflexible changes, making it difficult to apply to large-scale sensor deployment scenarios. Wan et al. [23] designed a 3-bit coded multiparameter reconfigurable RFID sensor, using p-i-n diodes to reconfigure the coding unit, improving the flexibility of coding, but there was a problem with limited coding information. A single structure can only encode "1" and "0," multibit coding requires a larger size, and the p-i-n diode consumes a large current, making it difficult for the system to achieve low power consumption. Therefore, the size and coding capacity of current RFID tags are the main challenges.

At present, RFID sensors have problems with inaccurate positioning and limited information in coding units. If wireless digital coding control technology can be applied to the SHM field, multibit coding is performed on a single coding unit, and information is obtained by changing the coding value of the sensor, it will significantly improve the sensor positioning capability.

In summary, traditional RFID sensors have the disadvantages of single detection parameters and limited coding information. At present, there is insufficient research on multiparameter RFID sensors that can simultaneously detect structural strain, humidity, and characterization coding in the field of structural measurement and control. There is no effective wireless control strategy for the frequency coding function of multiparameter sensors. Therefore, this article proposes a multiparameter RFID sensor that integrates low-cost digital control circuits, coding, humidity, and strain functions. In addition, a wireless dynamic control scheme is proposed, which provides new ideas for the intelligent network control scenario of multisensors.

A. Contributions

This article designs a novel RFID multiparameter sensor and proposes a method for wireless digital control of frequency coding. The main work is as follows.

1) A novel multiparameter RFID sensor was designed. In this sensor, two S-shaped structures are used for frequency coding units, one S-shaped structure is used for the humidity sensing unit, and a rectangular structure is used to implement the strain sensing unit. The coupling between the units was reduced through optimization, and the feasibility of the sensor and tag encoding was verified by High-Frequency Structure Simulator (HFSS) software.
2) The coding unit was optimized using varactor diodes, which expanded the amount of information carried by a single coding unit and greatly improved the flexibility of coding. The varactor diode was modeled using HFSS, and the working conditions of the coding structure under different states of the varactor diode were simulated.
3) A wireless digital control circuit was designed on the flexible printed circuit (FPC) to control the varactor diode and complete the digital control of the sensor frequency coding. At the same time, Bluetooth was used to wirelessly control the antenna frequency coding.
4) Experiments were conducted on the strain and humidity sensor to verify the feasibility of multiparameter detection. The effectiveness of frequency encoding by varactor diodes was verified through experiments.

II. RFID Sensor Based on Band-Stop Filter

This section proposes an RFID multiparameter sensor based on microstrip S-shaped and rectangular band-stop filters. The sensor consists of four different parts: a rectangular unit that measures strain by detecting the frequency shift caused by deformation, two S-shaped frequency encoding structures with varactor diodes, an S-shaped microstrip resonator structure with polyimide (PI) film for humidity monitoring, and a digital control circuit for receiving Bluetooth commands to control the coding value of the frequency coding bits.

A. Principle of Bend Structure in RFID Sensor

The bent structure is composed of several bend units, as shown in Fig. 1(a), where d is the length W is the width of the structure, and the arrow is the direction of the radiation current. The current flows in opposite directions in adjacent conductor segments in the normal direction of the bend, so their far-field radiation can cancel each other out. The current direction in the tangential direction is the same as the radiation direction, so when analyzing the radiation field of the meander structure, it can be simplified to a straight wire model, thereby reducing the difficulty of analysis.

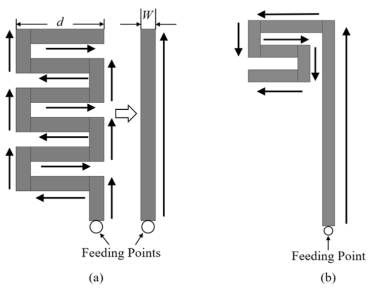

Fig. 1. (a) Bend structure. (b) S-shaped structure.

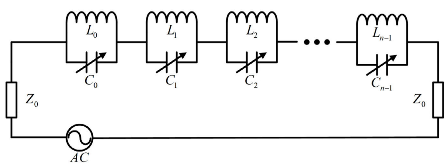

Fig. 2. Equivalent circuit of cascaded coding units.

The effective electrical length of a bent structure can be approximated as the sum of all conductor segments. Therefore, its effective electrical length is much larger than its radiation equivalent of a straight conductor, which can significantly reduce the overall structure size at the same resonant frequency. Its resonant frequency expression is

$$f_r = \frac{c}{2(L + 2\Delta L)\sqrt{\varepsilon_e}} \tag{1}$$

where f_r is the resonant frequency, c is the speed of light in vacuum, L is the sum of the lengths of all conductor segments, ΔL is the compensation length, and ε_e is the equivalent dielectric constant of the dielectric substrate. In order to reduce the size and maintain good band-stop characteristics, this article proposes an S-shaped structure based on the bent structure, which can better meet the above requirements. Its structure and radiation current are shown in Fig. 1(b).

The designed frequency encoding method is as follows: n encoding units are designed, and each encoding unit can perform m_1, m_2, $m_3, \ldots, m_n$-bit encoding. There is $m = m_1 \times m_2 \times m_3 \times \cdots \times m_n$-bit encoding in total, and the encoding working band is divided into mall sub-bands. When the resonant frequency of a tag falls into a sub-band, the encoding position corresponding to the sub-band is “1”; when the resonant frequency of no tag falls into the sub-band, the encoding position corresponding to the sub-band is “0.” When multiple encoding units are cascaded, they can be equivalent to a series of LC circuits in series, thereby generating notches at different resonant frequency points [24]. Considering that the varactor diode has the characteristic of variable capacitance, the equivalent circuit of multiple cascaded encoding units is shown in Fig. 2.

Advanced design system (ADS) software is used for simulation. The sensor is set to have four units, one of which is a coding unit that can perform 4-bit coding. The simulation results of the encoding principle by changing the capacitance value are shown in Fig. 3.

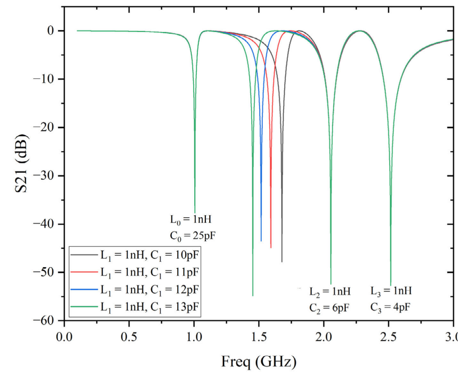

Fig. 3. Coding principle.

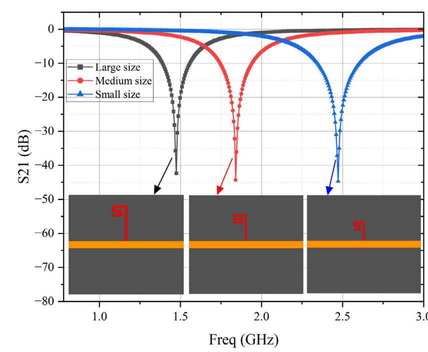

Fig. 4. S21 simulation results of S-shaped structures of different sizes.

Two encoding units are designed in this article, and each unit contains a varactor diode. By controlling the capacitance of the varactor diodes, the resonant frequency of the encoding unit can be controlled. In order to achieve RFID encoding and reduce coupling, appropriate sub-bands should be divided and appropriate resonant frequencies should be selected for each encoding unit. From (1), it can be seen that the resonant frequency is related to the effective electrical length. The shorter the effective electrical length, the higher the resonant frequency. Therefore, by adjusting the size of the S-shaped structure, different resonant frequencies can be obtained.

B. Multiparameter Sensor Design and Simulation

In order to integrate multiple S-shaped structures into one sensor, this article designs multiple S-shaped structures into different sizes so that the current propagation paths are different, resulting in different resonant frequencies. The forward transmission coefficient (S21) simulation results of S-shaped structures in different sizes are shown in Fig. 4.

It can be seen from Fig. 4 that the resonant frequencies of S-shaped structures in different sizes are different, and the smaller the size, the higher the resonant frequency.

The structure of the multiparameter sensor was obtained by combining a rectangular strain unit, two S-shaped frequency encoding units, an S-shaped humidity sensing unit, and a digital control circuit as shown in Fig. 5.

The digital control circuit is designed on the FPC board, which is attached to the substrate as a whole, and the bottom

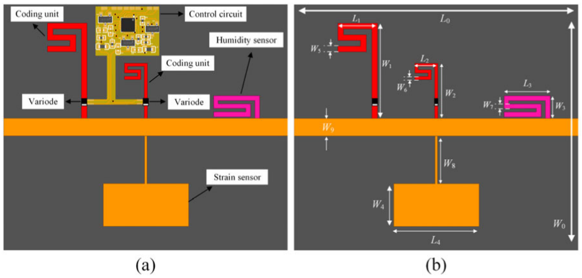

Fig. 5. Multiparameter sensor structure. (a) Composition. (b) Dimensions of the multiparameter sensor.

TABLE I
SENSOR STRUCTURE PARAMETERS

Parameter	L_0	L_1	L_2	L_3	L_4
Value(mm)	60	8.4	4.872	9.792	18
Parameter	W_0	W_1	W_2	W_3	W_4
Value(mm)	52	20	11.6	4.766	9
Parameter	W_5	W_6	W_7	W_8	W_9
Value(mm)	1.2	0.696	1.008	10	3.75

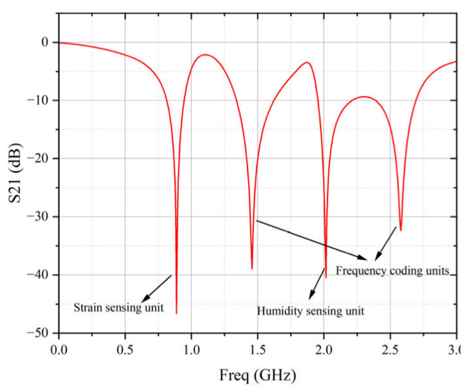

Fig. 6. S21 parameter simulation result of multiparameter sensor.

lead is connected to the pins of the two varactor diodes by welding. The parameters of the sensor are shown in Table I.

Fig. 6 shows the S21 resonance response curve obtained by optimizing the multiparameter sensor design in the RF simulation software HFSS. There are four resonance frequencies, 0.958, 1.51, 2.05, and 2.594 GHz, respectively.

In Fig. 6, the four resonant frequency points are generated by the resonance of two encoding units, one humidity sensing unit, and one strain unit. The four resonant frequency points are far apart, which can reflect a lower coupling degree.

C. Design of Digital Control Coding Part

The wireless digital control circuit system consists of a control circuit, Bluetooth, and varactor diodes and its structure is shown in Fig. 7.

The control circuit is designed on the FPC and has a bendable feature, which does not affect the performance of the strain sensor. The function of the digital control circuit is to control the reverse dc voltage value output to the varactor diode according to the command sent by Bluetooth, thereby controlling the capacitance of the varactor diode. The 10 V dc power supply outputs a 3.3 V voltage through a low dropout (LDO) regulator to power the microcontroller unit (MCU) and the Bluetooth module and is also connected to the collector of the n-p-n transistor. The MCU outputs a voltage signal with a peak-to-peak value of 3.3 V and an adjustable duty cycle through a pulsewidth modulation (PWM) module, and then raises the voltage to 10 V through an n-p-n transistor and outputs a dc voltage through a low-pass filter. The output dc voltage range is 0.1–10 V. The current-voltage output value is stored in the Flash inside the MCU. When the circuit is powered OFF and restarted, the output state before power failure is read from the Flash to achieve protection of state control.

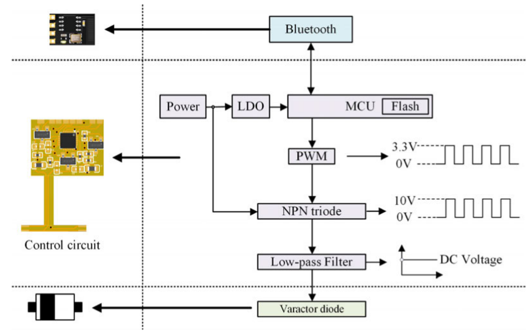

Fig. 7. Schematic of the wireless digital control circuit system.

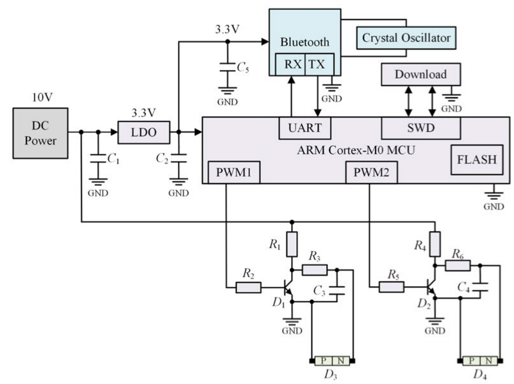

Fig. 8. Digital control circuit schematic.

The digital control circuit as a whole has the advantages of small size, low power consumption, and low cost. The main components include transistors, LDO, ARM Cortex-M0 core MCU, crystal oscillator as well as resistors, capacitors, and varactor diodes, with a total cost of approximately ten Chinese Yuan (CNY). The circuit schematic is shown in Fig. 8.

In Fig. 8, the MCU communicates with Bluetooth through the universal asynchronous receiver/transmitter (UART) peripheral and receives the control signal from the mobile phone. The function of capacitors C_1, C_2, and C_5 is to filter the power supply. Resistors R_3 and C_3 form a low-pass filter, and R_6 and C_4 form another low-pass filter. D_3 and D_4 are both varactor diodes, which are semiconductor devices made based on the principle of variable capacitance between p-n junctions. They are often used as variable capacitors in high-frequency

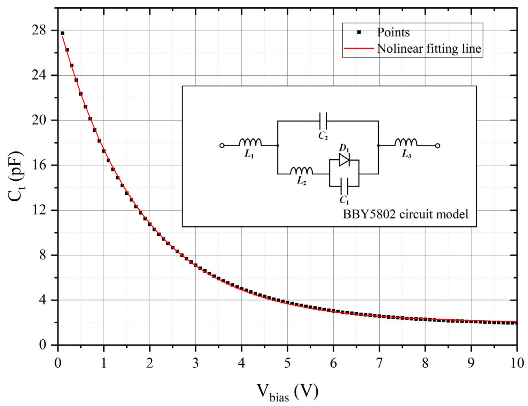

Fig. 9. Reverse voltage and capacitance curve of varactor diode.

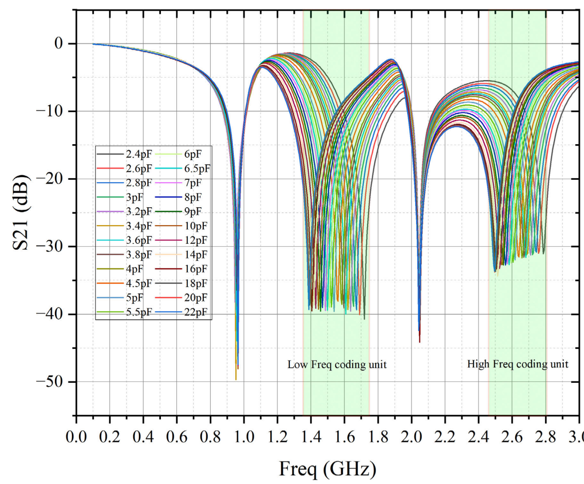

Fig. 10. S21 parameter simulation results under different capacitances.

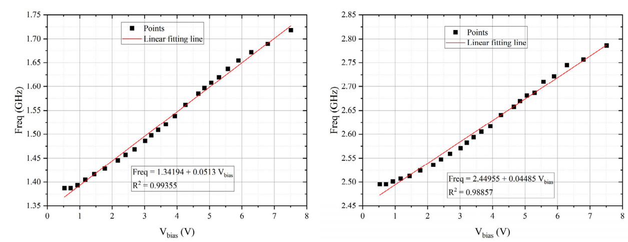

(a) (b)

Fig. 11. Relationship between the voltage and resonant frequency of the coding unit. (a) Low-frequency coding unit. (b) High-frequency coding unit.

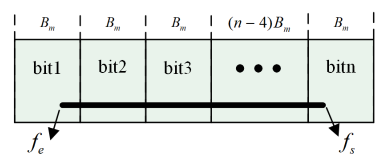

Fig. 12. Relationship between the number of codes and the resonant frequency.

tuning, communication, and other circuits to achieve reconfigurable or tuning functions [25]. Varactor diodes are reverse-biased diodes. Changing the reverse bias on their p-n junctions can change the capacitance of the p-n junction. The higher the reverse bias, the smaller the junction capacitance. The relationship between reverse bias and junction capacitance is nonlinear. This article uses a digital control circuit to apply different reverse voltages to the varactor diode and uses the controllable capacitance characteristics of the varactor diode to achieve multifrequency encoding of a single-frequency encoding unit.

The varactor diode used is BBY5802, and its SPICE model consists of one diode, one capacitor, and three inductors, as shown in Fig. 9. According to the SPICE model of the varactor diode, simulation is performed in ADS software to obtain the relationship between the applied reverse dc voltage and the capacitance and the fitting curve.

Within the voltage range of 0.1–10 V, the expression of reverse voltage and capacitance can be obtained through nonlinear fitting

$$C_t = 26.876 \times e^{\frac{-V_{\text{bias}}}{1.796}} + 1.99 \tag{2}$$

where C_t is the capacitance on both sides of the diode, V_{bias} is the input dc voltage, and the R^2 of the fitting curve is 0.99, which shows a good fitting effect. Then, the influence of the varactor diode on the two frequency coding units is simulated in HFSS. The varactor diode is simplified to be equivalent to a series connection of a variable capacitor and a resistor, where the resistor value is 0.25 Ω. The S21 parameter results of the multiparameter sensor under different capacitance values are shown in Fig. 10.

Fig. 10 shows that different capacitance values have a greater impact on the frequency of the encoding unit, and a smaller impact on the strain unit and humidity detection unit. The capacitance value of the varactor diode is continuously adjustable, so the corresponding reverse voltage is also continuous. Substituting different capacitance values into (2) to obtain the corresponding reverse voltage and extracting the resonant frequency values corresponding to different capacitances from the HFSS simulation results, the corresponding values of capacitance, reverse bias voltage, and resonant frequency are shown in Table II.

The reverse voltage and resonant frequency values of the low-frequency and high-frequency coding bits in Table II are fit, and the fitting curve is shown in Fig. 11.

For the low-frequency coding unit, the fitting curve is Freq $= 1.334194 + 0.0513\ V_{\text{bias}}$, the R^2 is 0.99355, which satisfies the linear relationship. The fitting curve of the high-frequency coding unit is Freq $= 2.44955 + 0.04485\ V_{\text{bias}}$, the R^2 is 0.98857, which also satisfies the linear relationship. According to the relationship between the reverse dc voltage and the resonant frequency of the coding unit, different voltage values can be used to control the coding value. The relationship between the number of codes and the resonant frequency is shown in Fig. 12.

Where f_s and f_e are the minimum and maximum values of the encoding unit resonant frequency, respectively, B_m is the bandwidth of the selected single code. The maximum number of codes m for a single coding bit satisfies the following

TABLE II
RELATIONSHIP BETWEEN VOLTAGE, CAPACITANCE, AND RESONANT FREQUENCY OF VARACTOR DIODE

C_t(pF)	2.4	2.6	2.8	3	3.2	3.4	3.6	3.8	4.0	4.5	5.0	5.5
V_{bias}(V)	7.512	6.799	6.29	5.89	5.57	5.29	5.056	4.845	4.657	4.258	3.932	3.656
f_l (GHz)	1.7182	1.689	1.6718	1.654	1.637	1.62	1.608	1.596	1.585	1.5616	1.538	1.521
f_h (GHz)	2.785	2.756	2.7448	2.722	2.71	2.687	2.681	2.669	2.658	2.640	2.617	2.606
C_t(pF)	6	6.8	7	8	9	10	12	14	16	18	20	22
V_{bias}(V)	3.417	3.206	3.017	2.69	2.414	2.174	1.774	1.447	1.17	0.93	0.719	0.53
f_l (GHz)	1.509	1.498	1.486	1.469	1.457	1.446	1.428	1.417	1.405	1.393	1.388	1.388
f_h (GHz)	2.594	2.582	2.571	2.559	2.548	2.536	2.5244	2.5128	2.507	2.5012	2.4954	2.4954

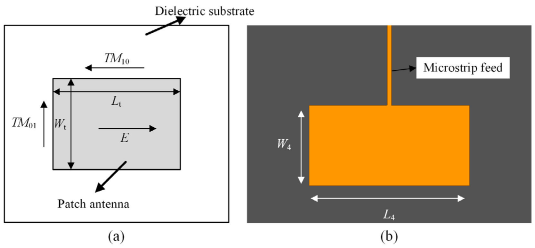

Fig. 13. (a) Patch antenna transmission line model. (b) Strain unit structure.

expression:

$$m = \mathrm{ceil}\left(\frac{f_s - f_e}{B_m}\right) + 1 \tag{3}$$

where ceil() is the upward rounding function.

D. Strain Sensing Unit Analysis and Simulation

This section uses a rectangular microstrip patch antenna sensor as a strain sensing unit and derives the normalized antenna resonant frequency offset based on the transmission line model. The HFSS simulation shows that the strain is linearly related to the frequency, which provides a theoretical basis for subsequent experimental verification. Fig. 13 shows the transmission line model diagram and circuit model of the rectangular patch.

The resonant frequency of the rectangular patch antenna in TM_{10} mode is

$$f_r = \frac{c}{4(L_t + \Delta L_t)\sqrt{\varepsilon_e}} \tag{4}$$

where c is the speed of light in a vacuum and ε_e is the effective dielectric constant of the medium. Since there is air above the metal patch and a medium below it, its electric lines will pass through different dielectric materials, causing a deviation between the theoretical size and the actual geometric size. The difference is the compensation length ΔL_t, which is calculated as follows:

$$\Delta L_t = 0.412h\frac{\varepsilon_e + 0.3}{\varepsilon_e - 0.258} \times \frac{w/h + 0.264}{w/h + 0.813}. \tag{5}$$

When the antenna is subjected to stress in the length direction, it will be stretched or compressed, and strain ε_L will be generated. The width of the metal patch and the thickness of the medium will change. When Poisson's ratio of the metal patch and the medium is the same, after the stress generates strain ε_L, the ratio of the width and thickness of the metal patch is approximately equal to that before the strain is generated, which is a constant.

From (7), we can see that when ε_e and the ratio of width to thickness do not change, ΔL_t is only related to the thickness h of the dielectric substrate, and the two are linearly related. Stress will cause the length L and thickness h of the antenna to change. Let the antenna length before the change be L_0, and the thickness of the dielectric be h_0, then the length and thickness of the metal patch after stress become

$$L_1 = L_0(1 + \varepsilon_L) \tag{6}$$

$$h_1 = h_0(1 - \upsilon_s\varepsilon_L). \tag{7}$$

The Poisson's ratio of the dielectric substrate is υ_s, and the relationship between the strain ε_L and the resonant frequency offset Δf is

$$\frac{\Delta f}{f_r} = -\frac{L_0 + C_2h_0}{L_0 + \upsilon_s C_2 h_0} * \varepsilon_L. \tag{8}$$

It can be seen from (10) that the resonant frequency offset Δf is linearly related to the strain ε_L. Let K be the antenna sensitivity, which represents the degree of frequency offset under each microstrain. The relationship between Δf and ε_L can be simplified as follows:

$$\frac{\Delta f}{f_r} = K\varepsilon_L. \tag{9}$$

The derivation in TM_{01} mode is similar to the previous one. When the excitation position is different, the working mode of the patch is different. It can be seen from (11) that the partial normalized antenna resonant frequency offset of the rectangular patch is linearly proportional to the strain, and due to the Poisson effect, the coefficient is negative. Based on the above theoretical derivation, a simulation experiment was carried out in the simulation software HFSS. The strain factor k was used as the variable parameter to scan the designed integrated sensor for reference to simulate strain stretching. The simulation results are shown in Fig. 14. It can be seen that the resonant frequency of the strain unit decreases monotonically, which is consistent with the theoretical derivation. In Fig. 15, the data are linearly fit to obtain Freq = 959.98–382.27k, $R^2 = 0.99396$.

E. Humidity Sensing Unit Analysis

When a large structure is in a high-humidity environment for a long time, the moisture in the environment will corrode the building materials, causing the building structure to be distorted or even collapse, shortening the life of the building

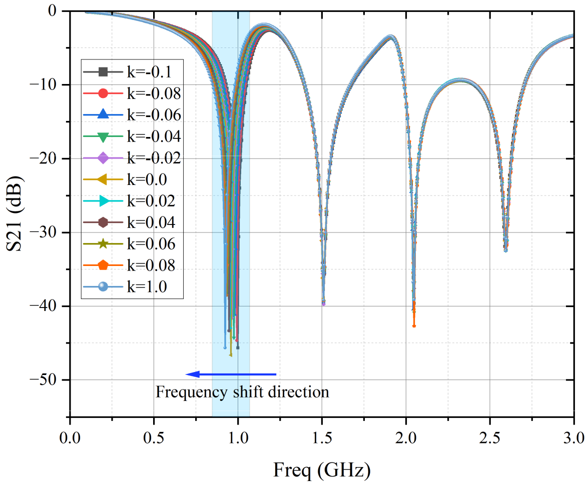

Fig. 14. Simulation results of S21 parameters under different strain factors.

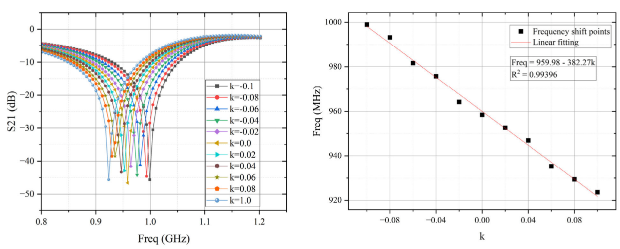

(a) (b)

Fig. 15. Simulation results and linear fitting line. (a) Simulation results after amplification. (b) Linear fitting of strain factor and resonant frequency.

structure. Therefore, humidity detection in a high-humidity environment is necessary in SHM.

PI is the abbreviation of PI, which has a series of imide rings on its main chain. Imide is a covalent compound containing a carbonyl group and an imide group formed by connecting an acyl group and an imide group through a double bond or a single bond. This conjugated system makes the imide have strong molecular polarity and hydrophilicity. Therefore, PI has humidity-sensitive properties. When the ambient humidity is low, there are fewer water molecules bound to the imide, and the dielectric constant of the PI film is relatively stable. As the ambient humidity gradually increases, the number of water molecules in the environment increases, and the probability of binding to the imide also greatly increases. Therefore, a large number of water molecules will be adsorbed onto the PI film to form an electric dipole-like structure, which will increase the dielectric constant of the PI film.

Based on the S-shaped structure, a humidity sensor for high humidity conditions is designed. The sensor part is made of Rogers RO3003 substrate with a thickness of 1.524 mm. The substrate is slightly affected by humidity. Based on the humidity-sensitive characteristics of PI, PI film can be used as a humidity-sensitive material to cover the surface of the humidity sensing unit. Since the electromagnetic wire of the humidity sensing unit will pass through the PI film, when the ambient humidity changes, the dielectric constant of the PI film changes, resulting in a shift in its resonant frequency. As the ambient humidity increases, the dielectric

TABLE III
ANTENNA PARAMETERS

Parameter	W_a	L_a	L_{gnd}	L_c
Value(mm)	100	100	27.4	1
Parameter	W_b	L_b	r_1	R_1
Value(mm)	2.86	29	6	35

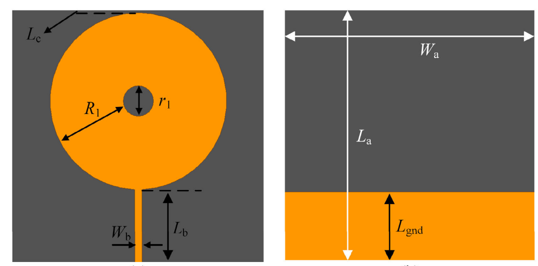

(a) (b)

Fig. 16. Antenna structure. (a) Front view. (b) Back view.

constant of the PI film increases, and the resonant frequency of the humidity sensing unit decreases. The resonant frequency is calculated as follows:

$$f_h = \frac{c}{2L_h\sqrt{\varepsilon_{\text{he}}}} \tag{10}$$

where c is the speed of light, L_h is the effective electrical length of the humidity sensor unit, and ε_{he} is the equivalent dielectric constant derived from the three dielectric constants [26]. The bending structure at the top of the S-shaped structure increases the transmission time of the RF signal, further improving the sensitivity of the humidity sensor unit to water molecules.

III. Experimental Verification of Sensor

A. Broadband Transceiver Antenna Design

The multiparameter sensor designed in this article has an operating frequency band of 0.96–2.6 GHz. A broadband antenna based on a circular ring shape is proposed for the transmission of wireless signals in this frequency band. The antenna has the advantage of good directivity. The substrate material is FR-4, and the thickness is 1.524 mm. Through iterative design of the inner circle radius, outer circle radius, and the overall size of the antenna, the final structure is shown in Fig. 16, and the antenna dimensions are shown in Table III.

The Input Reflection Coefficient (S11) results of the designed antenna by the network analyzer (vector network analyzer (VNA), Rohde and Schwarz ZVL, 9k–3 GHz) and simulation results are shown in Fig. 17. During simulation, the S11 parameters of the antenna are all below −10 dB in the 0.875–3 GHz frequency band. In actual measurement, the S11 parameters of the antenna are all below −10 dB in the 0.912–3 GHz frequency band. The measured result meets the requirement of the working frequency band.

B. Wireless Measurement Experiment

Both ends of the sensor are connected to the ultra-wideband (UWB) antenna designed in this article through the Sub

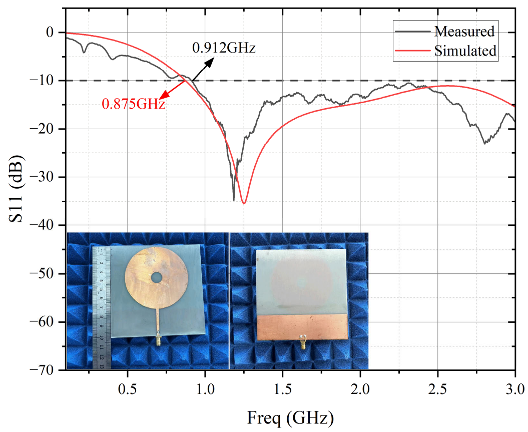

Fig. 17. S11 parameters of the designed antenna under simulation and measurement.

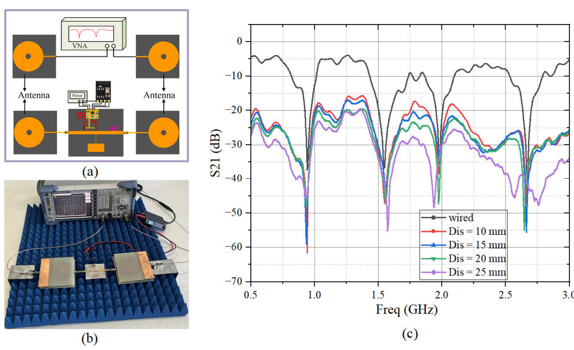

Fig. 18. S21 parameters of sensor underwired and wireless measurement. (a) Wireless detection system structure. (b) Experiment platform. (c) Experimental Results.

Miniature Version A (SMA) interface, and the antenna is universally connected at both ends of the VNA to verify the feasibility of contactless reading. The test environment and results are shown in Fig. 18. The receiving frequency of the sensor is accurately detected within a distance of 20 mm. At a distance of 25 mm, the result deviation is large, indicating that the effective receiving distance is less than 25 mm.

C. Digital Control Coding Experiment

The coding principle was simulated above. This section will explain the experiment and results. The experimental platform structure and sensor structure are shown in Fig. 19. The experimental platform consists of VNA, dc power supply, sensor with coding control circuit, and mobile phone. The function of dc power supply is to provide power to the Bluetooth module and coding control circuit. When the mobile phone sends instructions via Bluetooth, the coding control circuit obtains the sent instructions through the Bluetooth module and controls the reverse voltage value across the two varactor diodes according to the instructions, thereby controlling the equivalent capacitance value of the varactor diode. In order to simplify the experimental process, the amplitude of the output voltage to the two varactor diodes is set to be the same each time. VNA is used to measure the S21 parameter, and

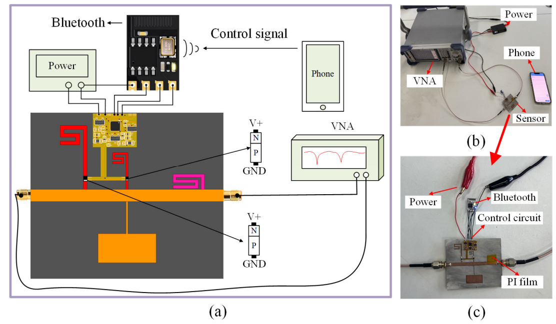

Fig. 19. Wireless control experiment of multiparameter sensor. (a) Overall structure of the experimental platform. (b) Physical picture of the experimental platform. (c) Sensor structure.

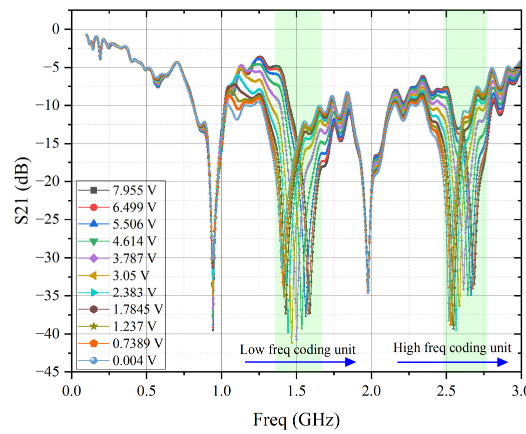

Fig. 20. S21 parameter results of digital control coding experiments.

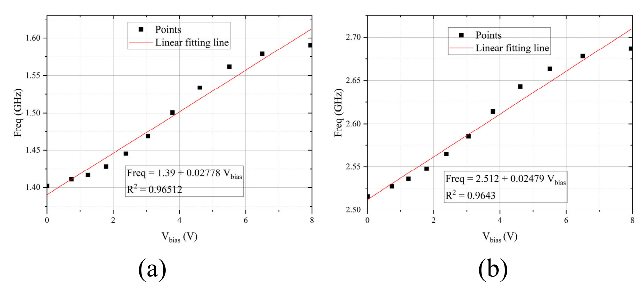

Fig. 21. Resonant frequency and voltage fitting curve of the frequency coding unit. (a) Low-frequency coding unit. (b) High-frequency coding unit.

the relationship between the voltage and the S21 parameter is shown in Fig. 20.

The voltage values and resonant frequency values of the low-frequency and high-frequency encoding units are fit, respectively, and the results are shown in Fig. 21. There is an obvious linear relationship between the resonant frequency and the reverse voltage, which is consistent with the simulation results. In the experiment, considering the resistance value at the connection of the varactor diode and the manufacturing error of the encoding unit structure, the frequency offset per voltage is smaller than the simulation result. For the low-frequency encoding unit, the determination coefficient R^2 is 0.96512, the frequency offset is 27.78 MHz/V when the voltage changes from 0.004 to 7.955 V. For the high-frequency encoding unit, R^2 is 0.9643, the frequency

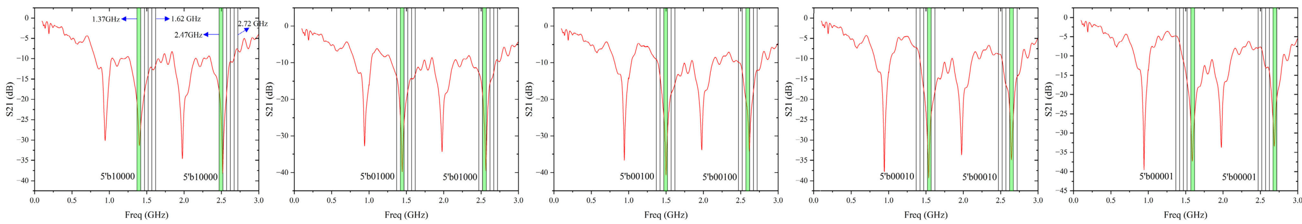

(a) (b) (c) (d) (e)

Fig. 22. Five typical encoding results of low-frequency coding unit and high-frequency coding unit. Both coding results are (a) "10000," (b) "01000," (c) "00100," (d) "00010," and (e) "00001."

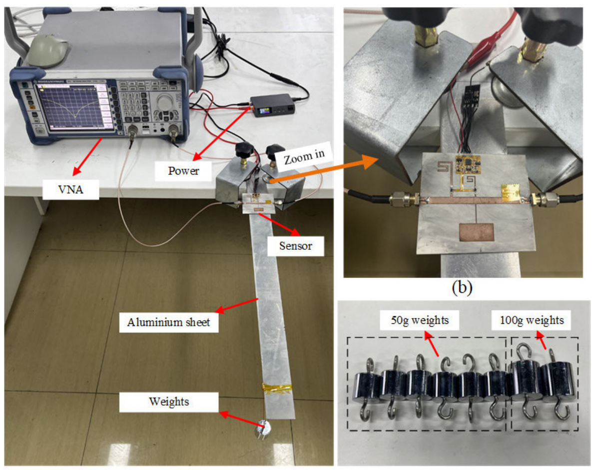

(a) (b) (c)

Fig. 23. (a) Strain experiment platform. (b) Sensor connected to the aluminum plate. (c) Weight.

offset is 24.79 MHz/V when the voltage changes from 0.004 to 7.955 V.

For RFID sensors, the traditional coding structure does not have a fixed bandwidth limit. It mainly considers the distance between the coding unit and the adjacent resonant frequency point to reduce the influence between different units. The two coding bits designed in this article are quite different from the adjacent resonant frequency points to avoid mutual influence. For a single coding bit, the bandwidth is set to 50 MHz, and the two designed coding structures can perform up to $5 \times 5 = 25$ bits of encoding. Five typical encoding results are shown in Fig. 22.

In Fig. 22, five frequency bands are divided in the frequency range of 1370–1620 MHz and 2470–2720 MHz, and the bandwidth of each frequency band is 50 MHz. When the resonance point falls into a certain 50 MHz frequency band, the coding value of the bit is "1," and the coding value of other bits is "0." Taking Fig. 22(a) as an example, the low-frequency coding value is "10000" and the high-frequency coding value is also "10000."

D. Strain Experiment Design

The strain experimental platform constructed is shown in Fig. 23.

The experimental platform includes the designed multiparameter RFID sensor, VNA, aluminum plate to be tested, and weights. It contains six 50 g weights and two 100 g weights. In the strain experiment, the multiparameter sensor was glued to a cantilever beam made of aluminum plate. The cantilever beam was fixed at a certain height from the ground, and the other end was suspended in the air. A weight is hung on the other side of the aluminum plate, and the aluminum plate will deform, thereby applying stress to the strain sensor. When the mass of the weight at the suspended end increases, the stress also increases, causing the strain sensor to be stretched and the resonant frequency to change. The sensor is connected to the VNA via a radio frequency cable for data observation and recording. The stress on the strain sensor is [27]

$$\varepsilon_k = \frac{6\ \mathrm{mg}(L_c - d_c)}{E_{\mathrm{eff}} W_c t_c^2} \tag{11}$$

where m is the total mass of the weight at the suspended end. g is the acceleration due to gravity. L_c is the length of the aluminum sheet, which is 450 mm. d_c is the distance from the midpoint of the strain sensor width to the fixed end of the sheet, which is 45 mm. W_c is the width of the sheet, which is 35 mm. t_c is the thickness of the sheet, which is 1.5 mm. E_{eff} is the effective elastic modulus of the sheet, which is 70 GPa.

In the experiment, weights were gradually added to the suspended end, and the results were recorded using VNA after stabilization. According to (11), for every 50 g increase in the total weight, the strain increased by about 0.2204‰. The S21 parameters under different strains are shown in Fig. 24.

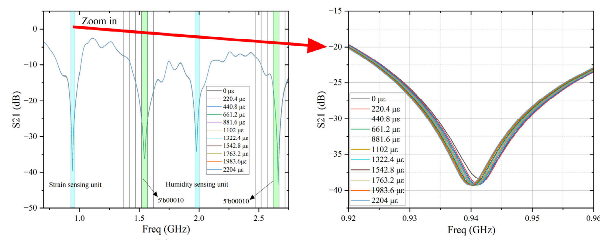

(a) (b)

Fig. 24. (a) S21 parameters measured under different strain. (b) S21 curve of the enlarged section.

In Fig. 24(a), the values of the two coding units are "00010" and "00010," respectively. As the strain changes, the coding values remain unchanged. The result of fitting the tensile data in the width direction is shown in Fig. 25.

In Fig. 25, there is an obvious linear relationship between the resonant frequency and the strain value. The fitting curve is Freq $= 941.377–7.4242 \times 10^{-4}\mu\varepsilon$, and the R^2 is 0.97832,

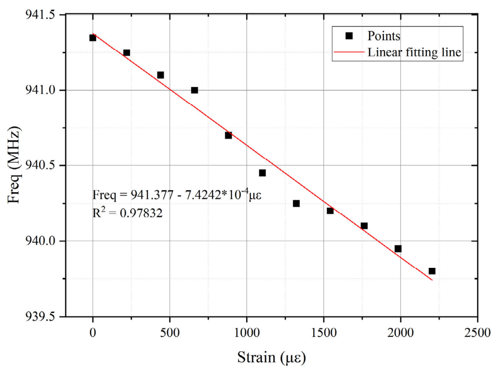

Fig. 25. Fitting relationship curve between strain and resonant frequency.

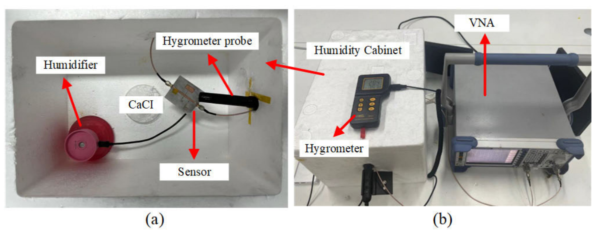

Fig. 26. (a) Components in the humidity chamber. (b) RH experimental platform.

indicating that the linear fitting effect is good, thus proving the feasibility of strain detection.

E. Humidity Experiment Design

In order to detect relative humidity (RH), the humidity sensing unit is covered with a PI film so that the sensor has humidity-sensitive characteristics. The PI film is pasted on the designed S-shaped humidity sensing unit with adhesive. The experimental equipment includes VNA, humidifier, hygrometer, calcium chloride anhydrous ($CaCl_2$) powder, and a sealable foam box. The specific experimental platform is shown in Fig. 26. Use the foam box to build a sealed humidity space, and punch holes in appropriate locations to allow the VNA data line, hygrometer probe, and humidifier power line to pass through. Then, change the humidity in the container through the humidifier, and after the hygrometer displays a stable value, measure the S21 parameter results under different humidity conditions. The powdered $CaCl_2$ is used to slow down the change of humidity, ensure that the PI film fully absorbs moisture, and avoid the humidity change too fast to affect the experimental test.

The measured S21 results of RH and resonant frequency are shown in Fig. 27.

In Fig. 27, as humidity increases, the resonant frequency of the humidity sensor unit decreases. At the same time, the code values of the two coding units are not affected, which are "10000" and "01000," respectively. The fitting result of the resonant frequency and humidity is shown in Fig. 28.

In Fig. 28, in the RH range of 33.7%–81.2%, the resonant frequency and RH change linearly, and the humidity sensitivity is 193.92 kHz/%RH, which shows the feasibility of the sensor.

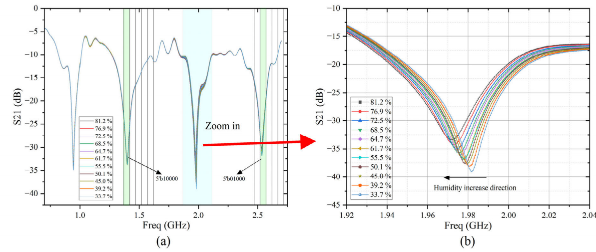

Fig. 27. (a) S21 parameters measured under different humidity. (b) S21 curve of the enlarged section.

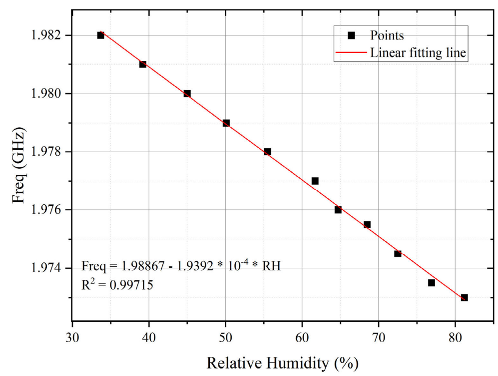

Fig. 28. Fitting relationship curve between RH and resonant frequency.

TABLE IV
COMPARISON OF CODING CHARACTERISTICS WITH OTHER STUDIES

Sensor ability	Coding unit number	Coding bit number	Coding adjustable	Power consumption	Ref.
Temperature Humidity	4	16	No	-	[19]
Humidity	3	8	No	-	[20]
Strain Humidity	3	8	Yes	High	[23]
Temperature Humidity	5	32	No	-	[28]
Strain	3	8	No	-	[29]
Strain Humidity	2	25	Yes	Low	This article

F. Encoding Ability Comparison

Table IV illustrates the literature on different RFID sensors with encoding functions. Compared with traditional encoding methods, the single encoding unit in this article has more encoding values and has an adjustable function.

When testing with a p-i-n diode, a single coding unit consumes about 10 mA of current when it is turned on at 0.85 V forward voltage. The varactor diode always works in the reverse state, and a single coding unit consumes less than 0.1 μA of current at 8 V reverse voltage. Therefore, the method of using a varactor diode has lower power consumption.

G. Discuss

This study integrated the coding, humidity, and strain functions by combining new organic materials, wireless digital control circuits, and varactor diodes, and designed an RFID sensor that can monitor strain parameters in building structures while acquiring coding and humidity data. The digital control circuit can control the capacitance value of the varactor diode through voltage, switch the coding value, and realize multifrequency coding on a single structure. The reverse voltage across the varactor diode is generally linearly related to the resonant frequency of the frequency coding structure. Increasing the coding value of the unit coding unit helps to provide more accurate sensor information, providing a feasible method for realizing multiparameter detection and reconfigurable functions in the SHM field.

The current integration is limited to two coding structures, resulting in limited capacity, but compared with the traditional single-structure 2-bit coding method, the number of codes has been greatly improved. Future optimization work can be to increase the number of structures, improve the coding capacity, and use multiple RFID sensors combined with software radio technology to build a large-scale SHM Internet of Things (IoT) system.

IV. Conclusion

This article designs a multiparameter RFID sensor for SHM, which realizes the integration of digital coding control, humidity, and strain detection functions. At the same time, a broadband transceiver antenna matching the working frequency band is designed. Experiments have shown that the change in the resonant frequency of the rectangular patch of the strain part is linearly related to the degree of strain; the humidity sensor can effectively detect RH. The frequency coding unit can realize multiple codes on a single coding structure through the control of varactor diodes and a digital control circuit, which improves the space utilization and information capacity of the sensor. Overall, the simultaneous monitoring of mechanical parameters and environmental parameters in the structure is achieved.

References

[1] C. A. Tokognon, B. Gao, G. Y. Tian, and Y. Yan, "Structural health monitoring framework based on Internet of Things: A survey," *IEEE Internet Things J.*, vol. 4, no. 3, pp. 619–635, Jun. 2017, doi: 10.1109/JIOT.2017.2664072.

[2] H. Huang and T. Bednorz, "Introducing S-parameters for ultrasound-based structural health monitoring," *IEEE Trans. Ultrason., Ferroelectr., Freq. Control*, vol. 61, no. 11, pp. 1856–1863, Nov. 2014, doi: 10.1109/TUFFC.2014.006556.

[3] O. Kypris and A. Markham, "3-D displacement measurement for structural health monitoring using low-frequency magnetic fields," *IEEE Sensors J.*, vol. 17, no. 4, pp. 1165–1174, Feb. 2017, doi: 10.1109/JSEN.2016.2636451.

[4] D. Lecompte, J. Vantomme, and H. Sol, "Crack detection in a concrete beam using two different camera techniques," *Struct. Health Monitor.*, vol. 5, no. 1, pp. 59–68, Mar. 2006, doi: 10.1177/1475921706057982.

[5] K. Mekki, O. Necibi, H. Dinis, P. Mendes, and A. Gharsallah, "Frequency-spectra-based high coding capacity chipless RFID using an UWB-IR approach," *Sensors*, vol. 21, no. 7, p. 2525, Apr. 2021, doi: 10.3390/s21072525.

[6] D. Jayawardana, S. Kharkovsky, and R. Liyanapathirana, "Measurement system with a RFID tag antenna mounted on structural members for infrastructure health monitoring," in *Proc. IEEE Int. Instrum. Meas. Technol. Conf. (I2MTC)*, Pisa, Italy, May 2015, pp. 7–12, doi: 10.1109/I2MTC.2015.7151231.

[7] X. Yi, C. Cho, J. Cooper, Y. Wang, M. M. Tentzeris, and R. T. Leon, "Passive wireless antenna sensor for strain and crack sensing—Electromagnetic modeling, simulation, and testing," *Smart Mater. Struct.*, vol. 22, no. 8, Aug. 2013, Art. no. 085009, doi: 10.1088/0964-1726/22/8/085009.

[8] A. Mita and S. Takhira, "A smart sensor using a mechanical memory for structural health monitoring of a damage-controlled building," *Smart Mater. Struct.*, vol. 12, no. 2, pp. 204–209, Apr. 2003, doi: 10.1088/0964-1726/12/2/307.

[9] Y. Watanabe, "Analysis of strain sensor using millimeter wave chipless RFID tag," in *Proc. Int. Symp. Antennas Propag. (ISAP)*, Osaka, Japan, Jan. 2021, pp. 45–46, doi: 10.23919/ISAP47053.2021.9391422.

[10] X. Yi, T. Wu, Y. Wang, and M. M. Tentzeris, "Sensitivity modeling of an RFID-based strain-sensing antenna with dielectric constant change," *IEEE Sensors J.*, vol. 15, no. 11, pp. 6147–6155, Nov. 2015, doi: 10.1109/JSEN.2015.2453947.

[11] G. Chakaravarthi, K. P. Logakannan, J. Philip, J. Rengaswamy, V. Ramachandran, and K. Arunachalam, "Reusable passive wireless RFID sensor for strain measurement on metals," *IEEE Sensors J.*, vol. 18, no. 12, pp. 5143–5150, Jun. 2018, doi: 10.1109/JSEN.2018.2831903.

[12] A. M. J. Marindra and G. Y. Tian, "Chipless RFID sensor tag for metal crack detection and characterization," *IEEE Trans. Microw. Theory Techn.*, vol. 66, no. 5, pp. 2452–2462, May 2018, doi: 10.1109/TMTT.2017.2786696.

[13] L. Xie, Z. Li, S. Xue, W. Lu, G. Wan, and W. Zang, "Effects of electrical contact on unstressed patch antenna sensors," *IEEE Sensors J.*, vol. 24, no. 10, pp. 16209–16219, May 2024, doi: 10.1109/JSEN.2024.3379581.

[14] C. Paggi, C. Occhiuzzi, and G. Marrocco, "Sub-millimeter displacement sensing by passive UHF RFID antennas," *IEEE Trans. Antennas Propag.*, vol. 62, no. 2, pp. 905–912, Feb. 2014, doi: 10.1109/TAP.2013.2292520.

[15] D. Jayawardana, S. Kharkovsky, R. Liyanapathirana, and X. Zhu, "Measurement system with accelerometer integrated RFID tag for infrastructure health monitoring," *IEEE Trans. Instrum. Meas.*, vol. 65, no. 5, pp. 1163–1171, May 2016, doi: 10.1109/TIM.2015.2507406.

[16] A. Moallemi, A. Burrello, D. Brunelli, and L. Benini, "Exploring scalable, distributed real-time anomaly detection for bridge health monitoring," *IEEE Internet Things J.*, vol. 9, no. 18, pp. 17660–17674, Sep. 2022, doi: 10.1109/JIOT.2022.3157532.

[17] S. Deif and M. Daneshmand, "Multiresonant chipless RFID array system for coating defect detection and corrosion prediction," *IEEE Trans. Ind. Electron.*, vol. 67, no. 10, pp. 8868–8877, Oct. 2020, doi: 10.1109/TIE.2019.2949520.

[18] M. Saban et al., "Sensing wood moisture in heritage and wooden buildings: A new sensing unit with an integrated LoRa-based monitoring system," *IEEE Internet Things J.*, vol. 9, no. 24, pp. 25409–25423, Dec. 2022, doi: 10.1109/JIOT.2022.3196740.

[19] L. Liu and L. Chen, "Characteristic analysis of a chipless RFID sensor based on multi-parameter sensing and an intelligent detection method," *Sensors*, vol. 22, no. 16, p. 6027, 2022, doi: 10.3390/s22166027.

[20] J. Hu, Y. Xie, G. Wan, and L. Xie, "A novel anti-interference encapsulated 3-bit coded RFID humidity sensor based on bent microstrip," *IEEE Trans. Instrum. Meas.*, vol. 73, pp. 1–10, 2024, doi: 10.1109/TIM.2024.3398133.

[21] A. Vena, E. Perret, and S. Tedjini, "Chipless RFID tag using hybrid coding technique," *IEEE Trans. Microw. Theory Techn.*, vol. 59, no. 12, pp. 3356–3364, Dec. 2011, doi: 10.1109/TMTT.2011.2171001.

[22] L. Chen, L. Liu, L. Kang, Z. Wan, G. Wan, and L. Xie, "A multibranch U-shaped tunable encoding chipless RFID strain sensor for IoT sensing system," *IEEE Internet Things J.*, vol. 10, no. 6, pp. 5304–5320, Mar. 2023, doi: 10.1109/JIOT.2022.3221938.

[23] G. Wan, Z. Jiang, and L. Xie, "A multiparameter integration method and characterization study of chipless RFID sensors with spiral shape," *IEEE Trans. Instrum. Meas.*, vol. 72, pp. 1–11, 2023, doi: 10.1109/TIM.2023.3306820.

[24] Y. J. Zhang, R. X. Gao, Y. He, and M. S. Tong, "Effective design of microstrip-line chipless RFID tags based on filter theory," *IEEE Trans. Antennas Propag.*, vol. 67, no. 3, pp. 1428–1436, Mar. 2019, doi: 10.1109/TAP.2018.2879854.

[25] S. A. Aghdam, "A novel UWB monopole antenna with tunable notched behavior using varactor diode," *IEEE Antennas Wireless Propag. Lett.*, vol. 13, pp. 1243–1246, 2014, doi: 10.1109/LAWP.2014.2332449.

[26] Z. Yi, S. Xue, L. Xie, and G. Wan, "Detection of setting time in cement hydration using patch antenna sensor," *Struct. Control Health Monitor.*, vol. 29, no. 1, pp. e285–5, Jan. 2022, doi: 10.1002/stc.2855.

[27] L. Wang, K. L. Chung, W. Zong, and B. Feng, "A highly sensitive microwave patch sensor for multidirectional strain sensing based on near orthogonal modes," *IEEE Access*, vol. 9, pp. 24669–24681, 2021, doi: 10.1109/ACCESS.2021.3056132.

[28] L. Kang, L. Chen, L. Liu, Z. Wan, G. Wan, and L. Xie, "Characteristics analysis of RFID multiparameter sensor tags based on various substrate materials," *IEEE Sensors J.*, vol. 23, no. 3, pp. 1875–1884, Feb. 2023, doi: 10.1109/JSEN.2022.3229467.

[29] G. Wan, M. Li, M. Zhang, L. Kang, and L. Xie, "A novel information fusion method of RFID strain sensor based on microstrip notch circuit," *IEEE Trans. Instrum. Meas.*, vol. 71, pp. 1–10, 2022, doi: 10.1109/TIM.2022.3161718.

Yaming Xie received the B.S. degree in microelectronics science and engineering from Northwest University, Xi'an, Shaanxi, China, in 2021, and the M.S. degree in microelectronics science and engineering from Tongji University, Shanghai, China, in 2023, where he is currently pursuing the Ph.D. degree in microelectronics science and engineering.

His current research interests include radio frequency identification (RFID) sensors and digital circuit design.

Jiuyi Hao received the B.S. degree in microelectronics science and engineering from Tongji University, Shanghai, China, in 2024, where she is currently pursuing the M.S. degree in microelectronics science and engineering.

Her current research interests include radio frequency identification (RFID) sensors and digital circuit design.

Zhichong Wan received the B.E. degree in electronic information engineering from Nanchang University, Nanchang, China, in 2019, and the M.S. degree in control science and engineering from Shanghai Institute of Technology, Shanghai, China, in 2023. He is currently pursuing the Ph.D. degree in microelectronics science and engineering with Tongji University, Shanghai.

His current research interests include machine learning and embedded development.

Guochun Wan received the Ph.D. degree in transportation information engineering and control from Tongji University, Shanghai, China, in 2011.

In 2006, he became an Associate Professor with the Department of Electronic Science and Technology, Tongji University. His current research interest focuses on sensitive electronics, radio frequency identification (RFID) sensors, circuit theory, and digital system design.

Liyu Xie received the B.S. and M.S. degrees in mechanical engineering from Tongji University, Shanghai, China, in 2000 and 2003, respectively, and the Ph.D. degree in system design engineering from Keio University, Tokyo, Japan, in 2009.

In 2019, he became an Associate Professor with the College of Civil Engineering, Tongji University. His current research focuses on smart sensors, structural health monitoring, and structural vibration control.